



Large-area grain-boundary-free copper films for plasmonics

Soo Hoon Chew^{a,b,c,1}, Alexander Gliserin^{a,b,c,1}, Sungho Choi^{b,c}, Xiao Tao Geng^{b,c}, Sujae Kim^d,
Woosup Hwang^e, Kangkyun Baek^e, Nguyen Duy Anh^f, Young-Jin Kim^f, Young Min Song^g,
Dong Eon Kim^{b,c}, Se-Young Jeong^{a,d,*}, Seungchul Kim^{a,h,*}

^a Department of Optics and Mechatronics Engineering, College of Nanoscience and Engineering, Pusan National University, 2 Busandaehak-ro 63beon-gil, Busan 46241, South Korea

^b Department of Physics, Center for Attosecond Science and Technology, Pohang University of Science and Technology, 77 Cheongam-Ro, Pohang 37673, South Korea

^c Max Planck Center for Attosecond Science, Max Planck POSTECH/Korea Research Initiative, 77 Cheongam-Ro, Pohang 37673, South Korea

^d Crystal Bank Research Institute, Pusan National University, 2 Busandaehak-ro 63beon-gil, Busan 46241, South Korea

^e Center for Self-assembly and Complexity, Institute for Basic Science, Pohang 37673, South Korea

^f School of Mechanical and Aerospace Engineering, Nanyang Technological University, 50 Nanyang Avenue, 639798 Singapore, Singapore

^g School of Electrical Engineering and Computer Science, Gwangju Institute of Science and Technology, Gwangju 61005, South Korea

^h Department of Cogno-Mechatronics Engineering, College of Nanoscience and Nanotechnology, Pusan National University, 2 Busandaehak-ro 63beon-gil, Busan 46241, South Korea

ARTICLE INFO

Keywords:

Single-crystalline films
Polycrystalline films
Copper
Surface plasmon resonances
Extraordinary optical transmission

ABSTRACT

Ultrasmooth single-crystalline metallic thin films provide several key advantages for the fabrication of well-defined and high-resolution plasmonic nanostructures, particularly complex integrated nanocircuits. For this purpose, copper is generally regarded as a poor plasmonic material compared to gold and silver because of its notorious oxidation issues when subjected to air exposure. Here, we report on the use of large-area grain-boundary-free copper films grown epitaxially on sapphire substrates in combination with focused ion beam milling to pattern plasmonic nanostructures with superior quality. The copper surfaces prepared using a single-crystalline copper sputtering target exhibit a very low roughness without any grain boundaries for varying film thicknesses and a strong resistance to oxidation, overcoming the bottleneck in conventional copper film fabrication. Surface plasmon resonance measurements show that improved dielectric constants with higher conductivity and long-term stability can be achieved using the single-crystalline copper films. Plasmonic nanohole arrays patterned from these high-quality films are found to display a stronger field enhancement compared to those made from polycrystalline copper films, thus resulting in an enhanced extraordinary optical transmission performance. This study suggests that our fabrication method is ideally suited for applications in copper-based plasmonic and nanophotonic devices as well as integrated nanocircuits on a large scale.

1. Introduction

Plasmonics, which explores the confinement of electromagnetic fields in subwavelength dimensions at metallic-dielectric surfaces, has emerged as a new frontier of science and engineering. A variety of fundamental and application-driven research activities based on plasmonics spanning from attosecond nanoplasmonics [1–3], highly efficient light sources [4–7] future-generation photovoltaic devices [8,9], ultrasensitive biochemical sensors [10–14] to integrated nanophotonic circuits [15–20] have been carried out at a breathtaking pace since the last decade and will continue to prosper towards a bright future. Silver

and gold, being the conventional plasmonic materials, have been widely used for applications in the range of visible and near-infrared (NIR) frequencies because of their well-researched surface chemistry [21,22] and relatively low optical losses [23]. Recently, aluminum has gained considerable interest owing to its capability of supporting surface plasmon resonance (SPR) in the ultraviolet region [24–26]. Compared to gold, silver and aluminum, copper has received much less attention in the plasmonic community because of its poor oxidation resistance [27–29] and high ohmic losses [18,30]. Notorious film oxidation such as Cu₂O and CuO [31–33] may already be formed throughout the film depth during the sputtering or evaporation process

* Corresponding authors at: Department of Optics and Mechatronics Engineering, College of Nanoscience and Engineering, Pusan National University, 2 Busandaehak-ro 63beon-gil, Busan 46241, South Korea.

E-mail addresses: syjeong@pusan.ac.kr (S.-Y. Jeong), s.kim@pusan.ac.kr (S. Kim).

¹ S. H. C. and A. G. contributed equally to this work.

<https://doi.org/10.1016/j.apsusc.2020.146377>

Received 29 January 2020; Received in revised form 20 March 2020; Accepted 3 April 2020

Available online 20 April 2020

0169-4332/ © 2020 The Authors. Published by Elsevier B.V. This is an open access article under the CC BY-NC-ND license (<http://creativecommons.org/licenses/by-nc-nd/4.0/>).

in the case of polycrystalline copper [34]. Moreover, surrounding oxygen atoms can diffuse quickly along the grain boundaries [34], which can cause higher oxygen incorporation into the films, thereby resulting in further degradation of the film quality. It has been shown that a thin oxide layer of 2–3 nm on the polycrystalline copper surface is already sufficient to reduce the surface plasmon polariton (SPP) propagation length by $\sim 50\%$ [35]. Different methods have been suggested and implemented to overcome copper oxidation including encapsulation of copper nanoparticles in a transparent matrix [36,37], oxide removal with glacial acetic acid [29,38], electrodeposition of transition metal shells onto copper nanowire films [39] and passivation layers on copper thin films [40–42]. However, some of these methods may introduce possibly undesirable changes of optical properties due to different materials added onto the copper surfaces, which in turn result in a shift of plasmon resonance as well as a change of local field enhancement.

Furthermore, fabricating copper nanodevices via electron beam lithography or focused ion beam (FIB) milling has been very difficult since polycrystalline copper films usually exhibit randomly oriented crystal grains [34,43] and grain boundary effects [34,35,44]. Surface roughness due to these random crystal grains and grain boundaries can directly lead to uneven cuts and structural defects in the process of copper device patterning [43,45]. Optical quality, i.e., the maximum value of achievable near-field intensity enhancement and spectral peak position of SPR, is therefore compromised as a result of imperfect nanostructures in terms of shape [46]. Additionally, increased scattering and damping of the surface plasmons can occur at the crystal defects or grain boundaries [35,47–49], which lower the efficiency of plasmon propagation and enhancement. Nevertheless, there are several key benefits in using copper as a constituent plasmonic material if the aforementioned issues of surface quality are solved. Copper is inexpensive in comparison to gold and silver because of its abundance in the earth's crust, allowing real-world practical applications, e.g., futuristic and large-scale plasmonic integrated circuits and nanophotonics which are compatible with industry-standard complementary metal-oxide semiconductor (CMOS) technology. From the perspective of plasmonics, copper's dielectric constants are comparable to gold around the optical wavelengths particularly in the range of 600–750 nm [50], which makes it a good candidate to replace gold for plasmonic applications. Besides, copper has the second-best conductivity after silver among the metals, another attractive property which has prompted its wide usage as interconnects in CMOS and electronics. Due to these reasons, several attempts have recently been made to integrate copper as a plasmon-supporting material into CMOS and silicon photonics. Remarkably efficient electro-optical coupling and low propagation loss in the telecommunication spectral range were achieved with a careful waveguide design [15,18,51].

Standard metallic thin films for plasmonic applications are typically prepared using thermal evaporation or sputtering techniques, which are polycrystalline in nature. In fact, all polycrystalline metallic films inherently experience the critical issues of surface quality including smooth template-stripped metallic films [49], and thus atomically flat single-crystalline metallic films and flakes [25,46,49] have been proposed several years ago for achieving precisely patterned plasmonic nanodevices. These reported high-definition plasmonic nanodevices are fabricated from single-crystalline gold, silver as well as aluminum, and so far no studies have been done on patterned single-crystalline copper nanodevices. Here, we demonstrate the use of large-area single-crystalline copper thin films with high quality in combination with FIB milling to achieve enhanced plasmonic devices. We employed a radio-frequency sputtering technique and a single-crystalline target instead of the more commonly used molecular beam epitaxy technique for growing atomically flat copper thin films on lattice-matched sapphire substrates.

2. Methods

2.1. Preparation of single-crystalline copper thin films

The single-crystalline copper thin films were grown on $10\text{ mm} \times 10\text{ mm}$ sapphire substrates with a thickness of 500 μm by a home-built radio-frequency sputtering machine [34]. The sputtering target, which is critical to produce a single-crystalline structure, is a sliced single-crystalline copper ingot. The sputtering was performed at a working pressure of $\sim 10^{-1}\text{ Pa}$ using an argon gas while the base pressure of the system was maintained at $\sim 10^{-3}\text{ Pa}$. A film growth rate of $\sim 0.1\text{ nm s}^{-1}$ and a deposition temperature of $150\text{ }^{\circ}\text{C}$ were used to achieve the optimal fabrication condition.

2.2. Preparation of polycrystalline copper thin films

For the study of SPR, approximately 69-nm-thick polycrystalline copper thin films were deposited on 500- μm -thick sapphire substrates with a growth rate of 0.1 nm s^{-1} using electron beam evaporation (KVE-4000, Korea Vacuum Tech) at room temperature. During the process of deposition, the pressure in the system was maintained at $\sim 7 \times 10^{-4}\text{ Pa}$. The 100-nm-thick polycrystalline copper thin films deposited on 500- μm -thick sapphire substrates for the extraordinary optical transmission (EOT) experiments were prepared using direct-current magnetron sputtering (SRN-110, SORONA); the sputtering system was kept at a base pressure of $\sim 1 \times 10^{-5}\text{ Pa}$. The films were sputtered at an argon pressure of $\sim 0.1\text{ Pa}$ with a growth rate of 1.4 nm s^{-1} .

2.3. TEM, AFM and SEM/EDS characterizations

The high-resolution analytical transmission electron microscope (TEM) measurement was performed using a Tecnai TF30 ST (FEI) system at an acceleration voltage of 300 kV. For TEM sample preparation, a FIB (Helios, 450 F1) was used. The atomic force microscope (AFM) images detailing the surface roughness and thickness of copper thin films were obtained using commercial AFM systems (XE-100 and NX10, Park Systems, Inc.). The scanned areas ($10\text{ }\mu\text{m} \times 10\text{ }\mu\text{m}$) of the samples were performed in non-contact mode at a scan rate of 0.5–0.7 Hz. The AFM measurements have an accuracy of $\pm 0.2\text{ nm}$. Energy dispersive X-ray analysis (EDS) was conducted by a field emission scanning electron microscope (SEM) (SUPRA 40 VP, Carl Zeiss) equipped with an EDS to examine the surface chemical composition of the EOT samples. The acceleration voltages for SEM and EDS were both set at 10 kV.

2.4. FIB milling

The nanohole arrays of the EOT experiments were fabricated on both single-crystalline and polycrystalline copper thin films using a FIB (Helios Nanolab G3 CX, FEI). An acceleration voltage of 30 kV and an ion beam current of 40 pA were used for the nanohole patterning on both thin films. The etched depth of the nanoholes was controlled by the ion milling time.

2.5. SPR setup

The SPR sensor consists of a copper thin film deposited on a sapphire substrate. The sapphire substrate was attached to a NS-F 11 prism (Edmund Optics, Inc.) using a non-drying immersion oil (MOIL-20LN, Leica Type N). The prism is chosen such that its refractive index is similar to that of the sapphire substrate. The sensor was fixed on a θ – 2θ motorized rotation stage (K10CR1/M, Thorlabs, Inc). The excitation source is a p-polarized 632.8 nm He-Ne laser (HNL050, Thorlabs, Inc) with an output power of 5 mW. A beam splitter was inserted in the input optical path to transmit 10% of the laser power to the sample with the rest being reflected onto a photodiode (DET36A/M, Thorlabs, Inc)

for power referencing. The angle of incidence was varied at step sizes of 0.01–0.1° by rotating the stage which was connected to a stepper motor driver. The angle-dependent reflectance from the prism with the copper film was measured by a power meter (PM200 with photodiode sensor S120C, Thorlabs, Inc.). This SPR setup is shown in Fig. S1 in Supplementary Information. The error of the absolute angle measurement is < 0.02° given by the calibration of the reference angle based on the back-reflection of the laser beam from the prism. In addition, the SPR angle measurement of our setup has an accuracy of $\pm 0.004^\circ$ (standard deviation) by considering the precision and repeatability of the rotation stage. The accuracy of the SPR reflectance amplitude measurement is estimated to be $\pm 0.01\%$ (standard deviation) which is determined from a three-day measurement at the reflectance dip without long-term drift. This standard deviation has taken into account the systematic drifts (stray light, dust on the sample and drift of the detectors) and statistical noise (laser power noise and electronic noise in the detectors).

2.6. EOT setup

Linearly polarized light from a 75 MHz broadband Ti:sapphire femtosecond oscillator laser (Venteon Pulse: One, Laser Quantum) centered at a wavelength of 788 nm was employed for illuminating the nanohole samples. The laser beam with an average power of 30 mW was focused to a spot size of $\sim 60 \mu\text{m}$ at normal incidence angle onto the center of $90 \mu\text{m} \times 90 \mu\text{m}$ nanohole arrays. Each sample was mounted on a 3-axis translation stage for accurate alignment of the beam focusing. The transmitted laser beam after the sample was detected by an optical spectrum analyzer (AQ-6315E, Ando) via a fiber optic. The experiments were performed under ambient conditions. The setup is illustrated in Fig. S2 in Supplementary Information.

2.7. Theoretical modeling of SPR

A simple SPR system consisting of three layers (prism, metal and air) based on the Kretschmann configuration is assumed in our modeling. For convenience of calculation, the prism is replaced by a sapphire substrate since they have almost the same refractive index at an excitation wavelength of 632.8 nm. A sapphire substrate, a copper film and air are abbreviated as s, c and a, respectively. The SPR is excited by totally reflected p-polarized light at the copper-air interface when the wave vector k_x of the incident light in the plane of the surface matches the wave vector k_0 of the SPP at the interface. The SPR can be analyzed by evaluating the reflectance R of the light following the three-layer Fresnel equation [52]:

$$R = \left| \frac{r_{sc} + r_{ca} \exp(2ik_{cz}d)}{1 + r_{sc}r_{ca} \exp(2ik_{cz}d)} \right|^2 \quad (1)$$

with

$$r_{sc} = \frac{k_{sz}\epsilon_c - k_{cz}\epsilon_s}{k_{sz}\epsilon_c + k_{cz}\epsilon_s} \quad (2)$$

$$r_{ca} = \frac{k_{cz}\epsilon_a - k_{az}\epsilon_c}{k_{cz}\epsilon_a + k_{az}\epsilon_c} \quad (3)$$

$$k_{jz} = \left(\epsilon_j \frac{\omega^2}{c^2} - k_x^2 \right)^{\frac{1}{2}} \text{ for } j = s, c, a \quad (4)$$

$$k_x = n_s \frac{\omega}{c} \sin \theta \quad (5)$$

where r_{sc} and r_{ca} are the reflectance amplitudes for sapphire-copper and copper-air interfaces, respectively; k_{jz} and ϵ_j are the wave-vector component perpendicular to the interface and the complex dielectric constant in medium j , respectively; d is the thickness of the copper film, ω and c are the angular frequency and speed of light, respectively; n_s is the refractive index of the sapphire; and θ is the angle of incidence of the light. The thickness d and complex dielectric function of copper ϵ_c are

optimized by a fitting algorithm for finding the best fit with the measurements in order to determine the effective optical constants and film thickness.

2.8. Theoretical modeling of EOT

A finite-difference time-domain (FDTD) method from Lumerical Solutions was employed to simulate the plasmonic near-field intensity distributions and transmitted spectra of the copper nanohole arrays on sapphire substrates used in the experiments. Three geometries with a copper film thickness of 100 nm, a hole diameter of 150 nm and different periodicities (550 nm, 600 nm and 650 nm) are modeled. A 2-nm-thick CuO layer on top of the copper nanohole arrays is considered to mimic the native oxidation formed on the copper film due to air exposure in the experiments. Periodic boundary conditions were applied to replicate a single unit cell of the nanohole array. A non-uniform mesh size was used with a highest accuracy of 0.5 nm. A plane wave source of a Gaussian profile having the same spectral width (600–1100 nm) as the broadband laser used in the experiments was used. The dielectric constants of copper are based on the handbook of CRC [53], while the dielectric constants of sapphire and CuO layer are taken from the handbook of E.D. Palik [54].

3. Results and discussion

3.1. Structural properties of single-crystalline copper films

The single-crystalline copper thin films were grown epitaxially on $10 \text{ mm} \times 10 \text{ mm}$ sapphire substrates by sputtering at a base pressure of $\sim 10^{-3} \text{ Pa}$ using an argon gas at 150°C and at a growth rate of $\sim 0.1 \text{ nm s}^{-1}$. Note that such a relatively high base pressure and low growth rate would usually result in uncontrolled oxidation of the metal surfaces during the deposition process. Despite this unfavorable condition, high-quality and oxidation-free copper thin films along the (111) direction with varying thickness can be easily achieved owing to the high chemical stability of the sputtered atoms from the single-crystalline target [34]. As depicted in Fig. 1(a), a perfectly regular and uniform lattice of the copper thin film is seen on top of the sapphire substrate in the TEM image. No crystal defects are seen in the image, inferring the high-purity and nearly perfect crystalline structure of the copper thin films. The single-crystallinity of the thin films was verified by selected-area electron diffraction using complementary electron backscatter diffraction in the TEM; Cu(111) was successfully grown in situ on the Al_2O_3 (0001) surface (see inset in Fig. 1(a)). The surface quality and morphology of the single-crystalline copper thin films were examined using an AFM. For comparison, we also deposited polycrystalline copper thin films on $10 \text{ mm} \times 10 \text{ mm}$ sapphire substrates via evaporation or sputtering. Fig. 1(b) and (c) show the representative AFM scanned areas of $10 \mu\text{m} \times 10 \mu\text{m}$ of both film surfaces with a film thickness of $\sim 50 \text{ nm}$. The surface of the single-crystalline copper film appears to be flat, continuous without any grains and grain boundaries whereas there are numerous randomly oriented grains (ranging in size from 30 to 100 nm) seen on the surface of the polycrystalline copper film. The root mean square (RMS) surface roughness values within the scanned area for the single- and polycrystalline copper films are 0.6 nm and 2.5 nm, respectively. In summary, we could achieve a very low RMS surface roughness in the range of ~ 0.2 – 0.6 nm for a single-crystalline copper film with a thickness of ~ 20 – 500 nm , a significant improvement of reduced surface roughness by approximately 15–46 times compared to a previously reported result [34]. The surface roughness values of our single-crystalline copper films are comparable to the values obtained in other works, i.e., $< 1 \text{ nm}$ for single-crystalline gold flakes [46], 0.82 nm and 1.30 nm for single-crystalline silver films with different thicknesses [49], and 0.3 nm for single-crystalline aluminum films [25] (Table S1, Supplementary Information). In contrast, the conventional evaporation or sputtering technique produces

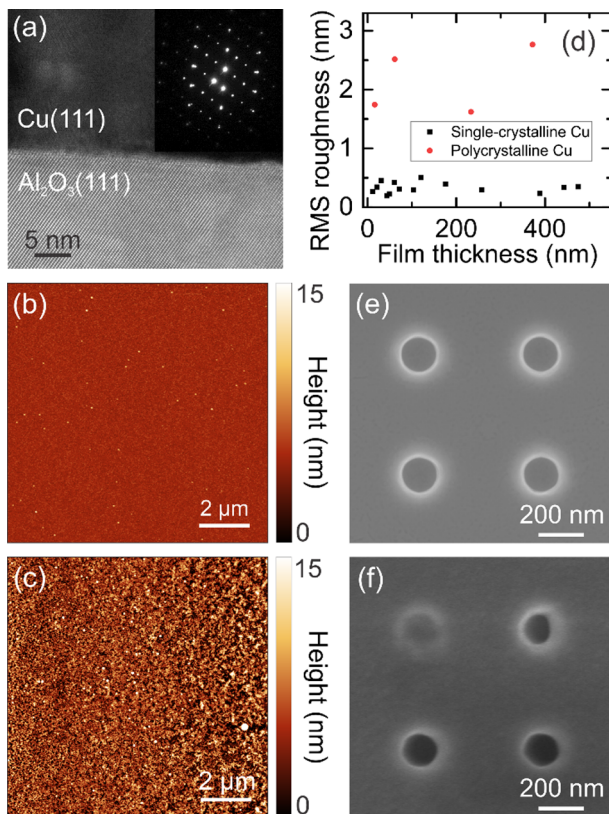


Fig. 1. Basic characterization of single-crystalline and polycrystalline copper (Cu) thin films on sapphire substrates. (a) High-resolution TEM image of a Cu/ Al_2O_3 sample with high crystallinity. Inset: electron backscatter diffraction pattern taken at the interface area between the copper film and the sapphire substrate. Representative AFM images showing the surface topography of (b) single-crystalline and (c) polycrystalline copper thin films. (d) Comparison of RMS surface roughness values for both films with varying film thicknesses. Representative SEM images of nanoholes with a diameter of 150 nm and a periodicity of 550 nm fabricated on (e) single-crystalline and (f) polycrystalline copper thin films using FIB milling before the experiments were performed.

polycrystalline copper films with much higher RMS surface roughness values for different thicknesses (Fig. 1d). Remarkably, a RMS surface roughness lower than 0.2 nm is attainable for all single-crystalline copper film thicknesses under stringently-controlled conditions. Such superior surface quality independent of film thickness is of key importance for multidisciplinary applications which require different thicknesses. High-precision copper nanostructures with ultrasoft surfaces are subsequently patterned by FIB milling. Fig. 1(e) and (f) show a comparison of nanofabrication quality via SEM imaging between using the single-crystalline and polycrystalline copper films, respectively. The nanoholes have a diameter of 150 nm and a periodicity of 550 nm, milled by FIB into a 100-nm-thick copper film on a 500- μm -thick sapphire substrate. Very fine structural features without any defects can easily be reproduced over a large area on the single-crystalline film whereas irregular edges of holes and unmilled holes are found on the polycrystalline film. It is well understood that the imperfect and imprecise nanostructures fabricated from polycrystalline films are caused by the presence of surface roughness, which consists of random grains and grain boundaries. This accounts for the fact that the etch rate differs for different grains [43] hence leading to unequal milling depths of the patterned areas. It should be noted that the FIB patterning quality is unavoidably reduced a little but not significantly when the fabrication area becomes very large (i.e., 90 $\mu\text{m} \times 90 \mu\text{m}$ periodic square arrays of ~ 17000 nanoholes in total).

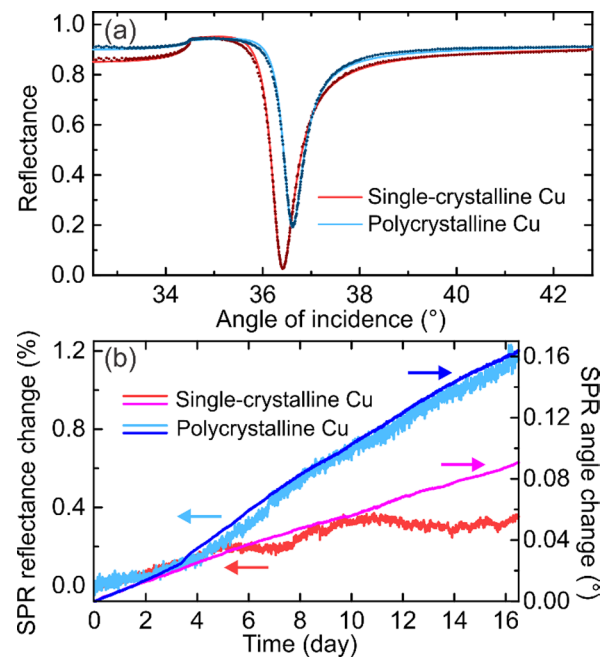


Fig. 2. Copper (Cu) SPR sensors and their long-term stability and performance. (a) SPR response curves for p-polarized laser light with a wavelength of $\lambda = 632.8$ nm. Theoretical fits (solid lines) to experimental data (dots) for both single-crystalline and polycrystalline copper thin films. (b) Measured SPR reflectance and angle changes at the resonance dip for both types of copper films.

3.2. SPR sensing of single-crystalline copper thin films

In order to demonstrate the improved optical properties of our single-crystalline copper films over polycrystalline copper films, we performed two plasmonic experiments, SPR and EOT using both types of films. In the SPR experiment, we applied the Kretschmann configuration [55–57] in angular interrogation mode under ambient conditions to excite SPP on the metal-dielectric interface (Fig. S1, Supplementary Information). SPR is a highly sensitive optical tool to measure a change in local refractive index of the medium by utilizing the enhanced electric field on the metal surface. This technique therefore finds use in a wide range of applications notably in chemical and biological sensing [56,58]. When the light beam propagates through the prism and encounters the interface between the copper thin film and air, an evanescent wave is formed and excites the SPP efficiently if the phase matching condition between the light wave and the surface plasmon is met. This condition is found by tuning the angle of incidence θ at the copper-air interface until a sharp minimum is seen in the reflected light. The measured reflectance of the copper film as a function of the angle of incidence θ is plotted as a response curve of the SPR sensor (Fig. 2(a)). The SPR measurements of single-crystalline and polycrystalline copper thin film samples were started about two weeks after the film fabrication. The measured thicknesses of the single-crystalline and polycrystalline copper films were (52.0 ± 0.5) nm and (68.7 ± 4.0) nm, respectively; both films were coated on 500- μm -thick sapphire substrates. Note that the reflectance losses at each interface were taken into account in the measured response curves by considering the Fresnel equations. In addition, power drift of the He-Ne laser used for excitation was corrected by referencing the measured reflected power to the input power during the entire measurements. The response curves of both copper sensors were analytically calculated using the Kretschmann configuration along with a three-layer Fresnel model to quantitatively determine the effective optical constants and thickness of the copper films (Fig. 2(a)). In our setup, the critical angle for total internal reflection is 34.5° as defined by the refractive index of sapphire. The theoretically fitted dielectric function and thickness are

$\epsilon_c = -11.72 + i0.71$ and $d = 51.8$ nm (single-crystalline copper film) and $\epsilon_c = -10.28 + i0.82$ and $d = 70.5$ nm (polycrystalline copper film) at 632.8 nm, respectively. Here, the effective thickness is the total thickness of the copper film and a thin native oxide layer [28] naturally grown on the copper film due to exposure to air. For the single-crystalline copper film, the calculated effective thickness (51.8 nm) agrees well with the measured thickness (52.0 nm). On the other hand, the discrepancy between the effective (70.5 nm) and measured (68.7 nm) thickness of the polycrystalline copper film might arise from severe oxidation on the film surface. The growth of an oxide layer is not self-limiting but can permeate into the grain boundaries and expand by consuming the polycrystalline copper film, rendering the entire film partially oxidized in the worst case. The simple theoretical model used in this work assumes a homogeneous metal film with an effective dielectric function and thickness and thus cannot account for intra-layer gradients of chemical composition. Explicit consideration of the oxide layer and composition gradient in a multilayer Fresnel model should more accurately reproduce the SPR response of severely oxidized copper films. However, this would require precise composition analysis of the oxide layer (e.g., by TEM after sectioning [59]), which is beyond the scope of this work. Nevertheless, our model is useful to extract trends of optical constants, which are attributed to changes in physical and chemical properties. As the film thickness increases from 52.0 nm to 68.7 nm, the SPR signal becomes weaker as predicted in the calculation (Fig. S3, Supplementary Information). However, the SPR dip does not shift to a smaller angle with an increased thickness as expected in Fig. S3. Instead, the SPR angle θ_{res} increases from 36.4° to 36.6° when the film thickness increases from 52.0 nm to 68.7 nm (Fig. 2(a)). The positive angle shift observed in the polycrystalline copper sensor is an indication of oxidation formed on the film surface as evidenced by similar observations reported before for other metal-deposited SPR sensors [60,61].

To further compare the robustness of both single-crystalline and polycrystalline copper films, the long-term stability of both SPR sensors under ambient conditions was monitored. The experimental results displaying the changes of the SPR dip reflectance and resonance angle over 16 days are shown in Fig. 2(b). These SPR changes are strongly dependent on the optical constants of the metallic film, such as the real ϵ' and imaginary ϵ'' parts of the complex dielectric function, besides the film thickness. The SPR dip reflectance values for both films increase at about the same rate for the first 5 days; however, the dip reflectance of the polycrystalline film rises much faster than that of the single-crystalline film afterwards. Furthermore, the dip reflectance change of the single-crystalline film slows down and only fluctuates slightly over time after the 5th day. The increase of dip reflectance (or decrease of the SPR signal) as a function of time indicates the plasmon coupling is reduced due to film degradation. In the meantime, the SPR angles for both films increase monotonically at about the same rate until the 2nd day and the angle change later escalates in the case of the polycrystalline film while it maintains the same rate for the single-crystalline film. On a short time scale of several minutes, both SPR sensors are very stable for real-time measurements as the changes of dip reflectance and angle are within or below the instrument errors of the system (0.01% and 0.004° for reflectance and angle, respectively, Fig. S4, Supplementary Information). As mentioned earlier, the changes of SPR properties reflect the evolution of the real part ϵ' and imaginary part ϵ'' of the complex dielectric function $\epsilon' + i\epsilon''$ of a metal film subjected to air exposure. $\epsilon' + i\epsilon''$ accounts for reflection and absorption of light in the metal. An analysis detailing the changes of the real and imaginary parts of the dielectric constants for both films over 16 days is shown in Fig. S5 in Supplementary Information. The effective dielectric constants of the single-crystalline and polycrystalline copper films change from $-11.72 + i0.71$ and $-10.28 + i0.82$ to $-11.22 + i0.68$ and $-9.63 + i0.79$, respectively, after 16 days. As illustrated in Fig. S5, it can be seen that ϵ' and ϵ'' of the polycrystalline film experience a bigger change than those of single-crystalline copper in the same period of

time. On the whole, the single-crystalline copper film exhibits dielectric constants with a larger negative ϵ' and a smaller ϵ'' than the polycrystalline copper film. A larger negative ϵ' implies a higher conductivity in a metal, by which a stronger excitation of collective oscillations of free charges can be induced by an external electromagnetic field due to the abundance of free conduction-band electrons. Meanwhile, a smaller ϵ'' indicates less absorption and therefore a lower energy loss of the SPPs propagating in the metallic film [62]. In addition, small damping of SPR is achieved if $|\epsilon'| \gg \epsilon''$ [28]. The single-crystalline copper SPR sensor exhibits a greater sensitivity since its $|\epsilon'/\epsilon''|$ ratio is 16.51, which is higher than that of the polycrystalline copper sensor, $|\epsilon'/\epsilon''| = 12.54$. After 16 days, the single-crystalline copper sensor has a negligible change of its sensitivity ($|\epsilon'/\epsilon''| = 16.50$) whereas it has decreased in the case of the polycrystalline copper sensor ($|\epsilon'/\epsilon''| = 12.19$). It has been demonstrated that oxide layers can contribute in broadening the SPR response curves [28,60]. Over the measurement period of 16 days, the full width at half maximum (FWHM) of the SPR dip increases from 0.64° to 0.67° (4.7% broadening) for the single-crystalline copper and from 0.54° to 0.59° (9.3% broadening) for the polycrystalline copper, respectively. This finding clearly reveals that the polycrystalline copper film is significantly more susceptible to surface contamination and oxidation in the ambient environment than the single-crystalline film. Consequently, these natural processes lead to increased surface roughness which can degrade the surface quality, manifesting in the change of the dielectric constants of the film. We found that the thickness of oxide layers on our single-crystalline copper films is usually self-limiting to a quasi-equilibrium value of 2 nm on top of the film surfaces, and more importantly, the oxygen does not penetrate into the films due to the absence of grain boundaries, unlike in the case of polycrystalline copper films. We also noticed that the high surface quality of a single-crystalline copper film is preserved after 6 months in contrast to a polycrystalline copper film where its RMS surface roughness has increased by ~200% after only 1 month of storage in ambient conditions (Fig. S6, Supplementary Information). Hence, the single-crystalline copper sensor proves to be much more stable and durable besides exhibiting a better SPR sensitivity performance compared to the polycrystalline copper sensor.

3.3. EOT through single-crystalline copper nanohole arrays

The exceptionally good surface quality of single-crystalline copper films enables us to fabricate reproducible subwavelength hole arrays that exhibit ultrasmooth surfaces and high-definition patterns for EOT experiments. A 100-nm-thick single-crystalline copper film on a 500- μm -thick sapphire substrate was perforated by a series of $90\ \mu\text{m} \times 90\ \mu\text{m}$ periodic square arrays of circular holes with a diameter of 150 nm and periods of 550 nm, 600 nm and 650 nm using a FIB. For comparison, another set of sample with the same design parameters was also fabricated on a 100-nm-thick polycrystalline copper thin film deposited on a 500- μm -thick sapphire substrate. The samples were illuminated with linearly polarized light with a central wavelength of 788 nm from a broadband Ti:sapphire oscillator, providing a wavelength range of 600–1100 nm which is essential for investigating the optical transmission spectra through the EOT samples (Fig. S2, Supplementary Information). The geometrical parameters (hole diameter, periodicity of the structure and copper film thickness) of the nanohole arrays are chosen such that the plasmon resonance is within our laser excitation wavelength range. The parameters are determined numerically by means of FDTD simulations. It has been shown that surface plasmon excitation of the nanohole array is primarily responsible for the light transmission through the holes with efficiencies larger than unity when normalized to the area of the holes [63,64]. The EOT mechanism can be briefly described as follows: Incoming photons are converted to SPPs on one side of the metal film, the SPPs propagate through the holes by tunneling, and then the SPPs scatter strongly at the hole edges and are reverted to photons on the other side of the film

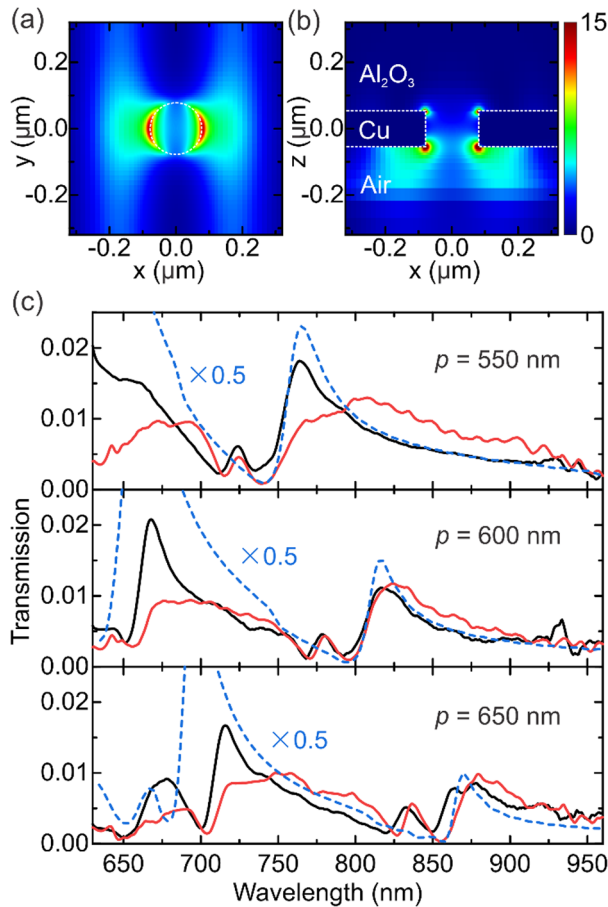


Fig. 3. Numerically simulated and experimental results of EOT samples. Exemplary simulated near-field intensity distributions of a copper (Cu) nanohole array sample (a) at the interface between air and copper and (b) from the side view at a resonant wavelength of 694 nm. The model geometry consists of a 100-nm-thick copper film with a hole diameter of 150 nm and a nanohole periodicity of 650 nm on a sapphire (Al₂O₃) substrate. The light polarization is parallel to the x-axis. The color bar shows the electric field intensity $|E|^2$. (c) Simulated and measured EOT spectra for three copper nanohole arrays with a film thickness of 100 nm, a hole diameter of 150 nm and varying periodicities, $p = 550$ nm, 600 nm and 650 nm. The dotted blue lines denote the simulated spectral transmissions while the solid black lines and solid red lines denote the transmission measurements of single-crystalline copper and polycrystalline copper samples, respectively. The simulated spectral transmissions are reduced by a factor of 2 for a better comparison with the lower experimental transmission values.

[65]. Fig. 3(a) and (b) depict the simulated intensity distributions around a nanohole in the periodic nanohole arrays by FDTD; the enhanced intensities are induced by the excitation of surface electromagnetic modes. Fig. 3(c) compares the simulated and measured zero-order transmission spectra through the nanohole arrays with varying periods (550 nm, 600 nm and 650 nm) at normal incidence. Note that the absolute transmission in the experiments is obtained by dividing the transmitted spectrum by the reference spectrum without the sample. A 2-nm-thick native oxide layer on top of the copper film is considered in the calculations. Overall, the simulated transmissions are higher than the experimentally observed transmitted intensities because the FDTD calculation does not take into account scattering losses which occur at the holes. Moreover, some variations in the hole diameter throughout the samples can be a contributing factor to the lower transmissions [65] observed in the experiments. In addition, the discrepancies in amplitude and minor deviations between the simulated and measured spectra can be attributed to the focusing condition in the experiments. This is because the EOT spectral features are strongly associated with the angle

of incidence of the incoming light [63,66] onto the sample.

It is well-known that the spectral peak position of the maximum transmission is related to the period of the nanohole arrays [63]. In our results, when the period increases from 550 nm to 650 nm, the peak positions are red-shifted accordingly, as shown in Fig. 3(c). These transmission peaks are attributed to the resonant features of localized surface plasmons and propagating SPPs in the holes and are dependent on the periodicity of the nanohole array, the specific order of the plasmon modes, and the dielectric function of the metal and its interfaces [67,68]. For period $p = 650$ nm, the minima in the experimental transmission curves at around 650 nm and 820 nm correspond to non-resonant Wood's anomalies [67] at the air and sapphire interfaces, respectively (see Fig. 3(c)). Wood's anomaly usually occurs in a diffractive array when the emerged beam is tangent to the array. Given by the period of the nanohole array, the minimum of the Wood's anomaly at the sapphire interface shifts correspondingly from 820 nm (for $p = 650$) to 770 nm and 710 nm (for $p = 600$ nm and $p = 550$ nm, respectively). The asymmetric line-shape of the transmission peaks is known as the Fano profile [69], marked by a rapid change of intensity when the Wood's anomaly is close to or interferes with the plasmon resonance. The Fano-like phenomenon in metallic nanohole arrays is most often observed when the hole size is small compared with the resonant wavelength and the metal film is thin [68], which is the case in our experiment. Aside from these discrepancies in amplitude and shape, the simulated spectra match reasonably well to the measured spectral features with respect to the spectral peak positions in the case of single-crystalline copper nanohole arrays for periods of 550 nm, 600 nm and 650 nm. It is to be noted that the transmission signals of the main peaks are lower by a factor of 2 in the polycrystalline nanohole arrays compared to the single-crystalline nanohole arrays for all periods. Besides that, the transmission peaks of the polycrystalline copper nanohole arrays appear to be less sharp and somewhat differently shaped in comparison to those of the single-crystalline copper nanohole arrays. In other words, the single-crystalline copper samples exhibit stronger and sharper plasmonic resonances, in fairly good agreement with the theoretical predictions. The observation of polycrystalline copper nanoholes with poorer transmission features, can well be due to structural imperfection of the nanoholes where not all unit cells are exactly identical, which is a common issue in polycrystalline metal films. Furthermore, increased SPP loss (e.g., reduced SPP propagation length) as a result of surface roughness in polycrystalline films can effectively degrade the EOT transmission [70].

3.4. SEM/EDX after experiments

Both single-crystalline and polycrystalline copper nanohole array samples were investigated for potential laser-induced contamination and oxidation after performing the EOT experiments. The sample surfaces were characterized and analyzed with a SEM equipped with EDS to obtain information about the surface morphology and chemical composition at specific locations within the region of interest (ROI). Fig. 4(a) and (b) show the SEM images of the single-crystalline and polycrystalline nanohole arrays, respectively, with a periodicity of 650 nm. The EDS spectra (Fig. 4(c–e)) were recorded for three ROIs shown in Fig. 4(a) and (b) and their corresponding atomic compositions and weight distributions are summarized in Table 1. No laser ablation on the surfaces is found since the laser peak intensity illuminated on the samples is $\sim 2 \times 10^9$ W cm⁻² (or a laser fluence of $\sim 4 \times 10^{-5}$ J cm⁻²), which is far below the laser damage threshold of metallic thin films [71]. However, several dark spots are visible on the surface of the polycrystalline sample which are mainly caused by adventitious carbon contamination originated from the adsorption of hydrocarbons, CO₂ or CO [72] in the ambient atmosphere. As shown in Table 1 and Fig. 4(b), the carbon concentration in terms of atomic percentage and weight percentage in ROI 3 (dark spot) is relatively higher than that in ROI 2 (without dark spot), confirming the aforementioned observation. At the

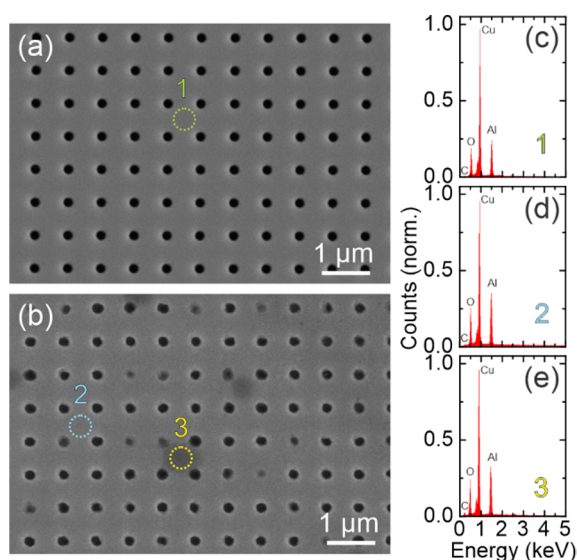


Fig. 4. SEM/EDS analysis of single-crystalline and polycrystalline copper nanohole samples after the EOT experiments. SEM images of (a) single-crystalline and (b) polycrystalline nanohole arrays with a periodicity of 650 nm used in the experiments before. The EDX spectra recorded at ROIs 1, 2 and 3 are shown in (c), (d) and (e), respectively. Elemental compositions of carbon (C), oxygen (O), copper (Cu) and aluminum (Al) are present in both films, see text for details.

Table 1

Atomic composition percentage (At%) and weight percentage (Wt%) of three ROIs (1, 2 and 3) from the single-crystalline and polycrystalline copper nanohole arrays shown in Fig. 4.

Element	1 ^a [At%]	2 ^b [At%]	3 ^b [At%]	1 ^a [Wt%]	2 ^b [Wt%]	3 ^b [Wt%]
C	3.69	2.75	6.66	1.11	0.89	2.17
O	24.59	27.44	24.86	9.87	11.80	10.79
Cu	44.10	37.36	37.19	70.31	63.78	64.13
Al	27.62	32.45	31.29	18.70	23.53	22.91

^a Single-crystalline copper nanohole arrays

^b Polycrystalline copper nanohole arrays

same time, carbon is also found on the single-crystalline copper surface. We conjecture that a uniform and thin adventitious carbon layer should form on the single-crystalline copper surface and remain in a normal state while carbon clustering can preferentially occur at the grain boundaries on the polycrystalline copper film. As a result, adventitious carbon contaminants appearing as dark spots are formed in the latter and continue to build up with increasing air exposure time. Heat generated from the laser illumination during the experiment should have exacerbated the surface contamination because this can weaken the nucleation sites, e.g., the grain boundaries or defects in the polycrystalline copper sample. In contrast, the single-crystalline copper film is usually more resistant to heat as it can withstand a high temperature of around 100–200 °C. Aluminum is detected in both copper films because the electron beam penetrated through the films and reached the sapphire substrates to excite the electrons within the aluminum compound. However, its amount is found to be higher in the polycrystalline copper sample in comparison to the single-crystalline sample. This is because the former exhibits a porous surface due to grain boundaries therefore the beam could penetrate deeper into the sapphire. In addition, a slightly higher oxygen amount is detected in the polycrystalline sample compared to the single-crystalline sample (see Table 1). It is presumed that the oxygen found in the polycrystalline sample originates from the oxide layer on top of the copper surface, the grain boundaries around the whole film and the sapphire. This is corroborated by a lower copper concentration in the polycrystalline film in comparison with the single-crystalline film.

4. Conclusions

We have demonstrated that epitaxially-grown copper films over large areas on sapphire substrates using a single-crystalline target are advantageous for plasmonic applications. Our single-crystalline copper films are shown to exhibit ultrasmooth surfaces which are less prone to oxidation and contamination in comparison to conventional polycrystalline copper films. In the SPR experiment, the single-crystalline copper film exhibits considerably improved dielectric constants with higher conductivity and lower absorption as well as greater durability compared to the polycrystalline copper film. Additionally, sharper EOT peaks along with stronger plasmonic resonances are observed in the single-crystalline copper nanohole arrays compared with the nanohole arrays fabricated from the polycrystalline copper film. This is attributed to reduced propagation loss of SPPs in the nanoholes due to their well-defined and smooth features. Our findings open an alternative pathway to the practical use of single-crystalline copper films in active and more complex plasmonic and nanophotonic devices as well as functional integrated nanocircuits in the industry.

CRediT authorship contribution statement

Soo Hoon Chew: Methodology, Formal analysis, Investigation, Validation, Writing - original draft, Writing - review & editing, Visualization. **Alexander Gliserin:** Methodology, Formal analysis, Investigation, Software, Writing - review & editing, Visualization. **Sungho Choi:** Formal analysis, Investigation. **Xiao Tao Geng:** Formal analysis, Investigation. **Sujae Kim:** Investigation, Resources. **Wooseup Hwang:** Investigation, Resources. **Kangkyun Baek:** Formal analysis, Investigation, Resources. **Nguyen Duy Anh:** Formal analysis. **Young-Jin Kim:** Formal analysis. **Young Min Song:** Writing - review & editing. **Dong Eon Kim:** Resources, Supervision, Project administration, Funding acquisition. **Se-Young Jeong:** Conceptualization, Methodology, Validation, Resources, Supervision, Project administration, Funding acquisition. **Seungchul Kim:** Conceptualization, Methodology, Validation, Writing - review & editing, Resources, Supervision, Project administration, Funding acquisition.

Declaration of Competing Interest

The authors declare that they have no known competing financial interests or personal relationships that could have appeared to influence the work reported in this paper.

Acknowledgements

We acknowledge T. Khurelbaatar for technical support. This work was financially supported by Creative Materials Discovery Program (NRF-2017M3D1A1039287), Basic Research Lab Program (NRF-2018R1A4A1025623), Young Researcher Program (NRF-2017R1C1B2006137), Basic Science Research Program (NRF-2017R1A2B3011822), in part by Global Research Laboratory Program (2009-00439) and Max Planck POSTECH/Korea Research Initiative Program (2016K1A4A01922028) through the National Research Foundation of Korea (NRF) funded by the Ministry of Science, ICT, and Future Planning, and Korea Institute for Advancement of Technology (KIAT) grant funded by the Korea Government (MOTIE) (P0008763).

Appendix A. Supplementary data

Supplementary data to this article can be found online at <https://doi.org/10.1016/j.apsusc.2020.146377>.

References

- [1] M.I. Stockman, M.F. Kling, U. Kleineberg, F. Krausz, Attosecond nanoplasmonic-field microscope, *Nat. Photon.* 1 (2007) 539–544.
- [2] A. Mikkelsen, J. Schwenke, T. Fordell, G. Luo, K. Klünder, E. Hilner, N. Anttu, A.A. Zakharov, E. Lundgren, J. Mauritsson, J.N. Andersen, H.Q. Xu, A. L'Huillier, Photoemission electron microscopy using extreme ultraviolet attosecond pulse trains, *Rev. Sci. Instrum.* 80 (2009) 123703.
- [3] S.H. Chew, F. Süßmann, C. Späth, A. Wirth, J. Schmidt, S. Zherebtsov, A. Guggenmos, A. Oelsner, N. Weber, J. Kapaldo, A. Gliserin, M.I. Stockman, M.F. Kling, U. Kleineberg, Time-of-flight-photoelectron emission microscopy on plasmonic structures using attosecond extreme ultraviolet pulses, *Appl. Phys. Lett.* 100 (2012) 051904.
- [4] R.F. Oulton, V.J. Sorger, T. Zentgraf, R.M. Ma, C. Gladden, L. Dai, G. Bartal, X. Zhang, Plasmon lasers at deep subwavelength scale, *Nature* 461 (2009) 629–632.
- [5] R.-M. Ma, R.F. Oulton, V.J. Sorger, G. Bartal, X. Zhang, Room temperature plasmon laser by total internal reflection, *Nat. Mater.* 10 (2010) 110–113.
- [6] G. Lozano, D.J. Louwers, S.R.K. Rodriguez, S. Murai, O.T.A. Jansen, M.A. Verschuuren, J. Gómez Rivas, Plasmonics for solid-state lighting: Enhanced excitation and directional emission of highly efficient light sources, *Light Sci. Appl.* 2 (2013) e66.
- [7] G. Lozano, S.R.K. Rodriguez, M.A. Verschuuren, J.G. Rivas, Metallic nanostructures for efficient LED lighting, *Light Sci. Appl.* 5 (2016) 1–10.
- [8] H.A. Atwater, A. Polman, Plasmonics for improved photovoltaic devices, *Nat. Mater.* 9 (2010) 205–213.
- [9] N.N. Lal, B.F. Soares, J.K. Sinha, F. Huang, S. Mahajan, P.N. Bartlett, N.C. Greenham, J.J. Baumberg, Enhancing solar cells with localized plasmons in nanovoids, *Opt. Express* 19 (2011) 11256–11263.
- [10] M.E. Stewart, C.R. Anderton, L.B. Thompson, J. Maria, S.K. Gray, J.A. Rogers, R.G. Nuzzo, Nanostructured plasmonic sensors, *Chem. Rev.* 108 (2008) 494–521.
- [11] J.N. Anker, W.P. Hall, O. Lyandres, N.C. Shah, J. Zhao, R.P. Van Duyne, Biosensing with plasmonic nanosensors, *Nat. Mater.* 7 (2008) 442–453.
- [12] Y. Lin, Y. Zou, R.G. Lindquist, A reflection-based localized surface plasmon resonance fiber-optic probe for biochemical sensing, *Biomed. Opt. Express* 2 (2011) 478.
- [13] Y. Hong, Y.M. Huh, D.S. Yoon, J. Yang, Nanobiosensors based on localized surface plasmon resonance for biomarker detection, *J. Nanomater.* 2012 (2012) 13.
- [14] C. Caucheteur, T. Guo, J. Albert, Review of plasmonic fiber optic biochemical sensors: improving the limit of detection, *Anal. Bioanal. Chem.* 407 (2015) 3883–3897.
- [15] C. Delacour, S. Blaize, P. Grosse, J.M. Fedeli, A. Bruyant, R. Salas-Montiel, G. Lerondel, A. Chelnokov, Efficient directional coupling between silicon and copper plasmonic nanoslot waveguides: Toward metal-oxide-silicon nanophotonics, *Nano Lett.* 10 (2010) 2922–2926.
- [16] V.J. Sorger, R.F. Oulton, R.M. Ma, X. Zhang, Toward integrated plasmonic circuits, *MRS Bull.* 37 (2012) 728–738.
- [17] M. Chamanzar, Z. Xia, S. Yegnanarayanan, A. Adibi, Hybrid integrated plasmonic-photon waveguides for on-chip localized surface plasmon resonance (LSPR) sensing and spectroscopy, *Opt. Express* 21 (2013) 32086.
- [18] D.Y. Fedyanin, D.I. Yakubovsky, R.V. Kirtaev, V.S. Volkov, Ultralow-Loss CMOS Copper Plasmonic Waveguides, *Nano Lett.* 16 (2016) 362–366.
- [19] J.-S. Shin, J.T. Kim, Broadband silicon optical modulator using a graphene-integrated hybrid plasmonic waveguide, *Nanotechnology* 26 (2015) 365201.
- [20] Y. Fang, M. Sun, Nanoplasmonic waveguides: Towards applications in integrated nanophotonic circuits, *Light Sci. Appl.* 4 (2015) e294.
- [21] P.C. Lee, D. Meisel, Adsorption and surface-enhanced Raman of dyes on silver and gold sols, *J. Phys. Chem.* 86 (1982) 3391–3395.
- [22] Y. Sun, Y. Xia, Shape-controlled synthesis of gold and silver nanoparticles, *Science* 298 (2002) 2176–2179.
- [23] M.G. Blaber, M.D. Arnold, N. Harris, M.J. Ford, M.B. Cortie, Plasmon absorption in nanospheres: A comparison of sodium, potassium, aluminium, silver and gold, *Phys. B Condens. Matter.* 394 (2007) 184–187.
- [24] M.W. Knight, N.S. King, L. Liu, H.O. Everitt, P. Nordlander, N.J. Halas, Aluminum for plasmonics, *ACS Nano* 8 (2014) 834–840.
- [25] H.W. Liu, F.C. Lin, S.W. Lin, J.Y. Wu, B.T. Chou, K.J. Lai, S. Di Lin, J.S. Huang, Single-crystalline aluminum nanostructures on a semiconducting GaAs substrate for ultraviolet to near-infrared plasmonics, *ACS Nano* 9 (2015) 3875–3886.
- [26] W. Li, K. Ren, J. Zhou, Aluminum-based localized surface plasmon resonance for biosensing, *TrAC Trends Anal. Chem.* 80 (2015) 486–494.
- [27] S. Suzuki, Y. Ishikawa, M. Isshiki, Y. Waseda, Native oxide layers formed on the surface of ultra high-purity iron and copper investigated by angle resolved XPS, *Mater. Trans.* 38 (1997) 1004–1009.
- [28] M. Mitsushio, K. Miyashita, M. Higo, Sensor properties and surface characterization of the metal-deposited SPR optical fiber sensors with Au, Ag, Cu, and Al, *Sens. Actuators A Phys.* 125 (2006) 296–303.
- [29] G.H. Chan, J. Zhao, E.M. Hicks, G.C. Schatz, R.P. Van Duyne, Plasmonic properties of copper nanoparticles fabricated by nanosphere lithography, *Nano Lett.* 7 (2007) 1947–1952.
- [30] A.V. Krasavin, A.V. Zayats, Silicon-based plasmonic waveguides, *Opt. Express* 18 (2010) 11791.
- [31] T.L. Barr, An ESCA study of the termination of the passivation of elemental metals, *J. Phys. Chem.* 82 (1978) 1801–1810.
- [32] J.C. Yang, B. Kolasa, J.M. Gibson, M. Yeadon, Self-limiting oxidation of copper, *Appl. Phys. Lett.* 73 (1998) 2841–2843.
- [33] J.H. Kim, S.H. Ehrman, T.A. Germer, Influence of particle oxide coating on light scattering by submicron metal particles on silicon wafers, *Appl. Phys. Lett.* 84 (2004) 1278–1280.
- [34] S. Lee, J.Y. Kim, T.W. Lee, W.K. Kim, B.S. Kim, J.H. Park, J.S. Bae, Y.C. Cho, J. Kim, M.W. Oh, C.S. Hwang, S.Y. Jeong, Fabrication of high-quality single-crystal Cu thin films using radio-frequency sputtering, *Sci. Rep.* 4 (2014) 6230.
- [35] H.S. Lee, C. Awada, S. Boutami, F. Charra, L. Douillard, R.E. de Lamaestre, Loss mechanisms of surface plasmon polaritons propagating on a smooth polycrystalline Cu surface, *Opt. Express* 20 (2012) 8974.
- [36] R.L. Zong, J. Zhou, B. Li, M. Fu, S.K. Shi, L.T. Li, Optical properties of transparent copper nanorod and nanowire arrays embedded in anodic alumina oxide, *J. Chem. Phys.* 123 (2005) 94710.
- [37] O.A. Yeshchenko, I.M. Dmitruk, A.A. Alexeenko, A.M. Dmytruk, Size-dependent melting of spherical copper nanoparticles embedded in a silica matrix, *Phys. Rev. B* 75 (2007) 85434.
- [38] K.L. Chavez, D.W. Hess, A novel method of etching copper oxide using acetic acid, *J. Electrochem. Soc.* 148 (2001) G640.
- [39] Z. Chen, S. Ye, I.E. Stewart, B.J. Wiley, Copper nanowire networks with transparent oxide shells that prevent oxidation without reducing transmittance, *ACS Nano* 8 (2014) 9673–9679.
- [40] C.S. Hsu, H.Y. Hsieh, J.S. Fang, Enhancement of oxidation resistance and electrical properties of indium-doped copper thin films, *J. Electron. Mater.* 37 (2008) 852–859.
- [41] O.S. Hutter, H.M. Stec, R.A. Hatton, An indium-free low work function window electrode for organic photovoltaics which improves with in-situ oxidation, *Adv. Mater.* 25 (2013) 284–288.
- [42] G. Zhao, W. Wang, T.-S. Bae, S.-G. Lee, C. Mun, S. Lee, H. Yu, G.-H. Lee, M. Song, J. Yun, Stable ultrathin partially oxidized copper film electrode for highly efficient flexible solar cells, *Nat. Commun.* 6 (2015) 8830.
- [43] J.D. Casey, M. Phaneuf, C. Chandler, M. Megorod, K.E. Noll, R. Schuman, T.J. Gannon, A. Krechmer, D. Monforte, N. Antoniou, N. Bassom, J. Li, P. Carleson, C. Huynh, Copper device editing: Strategy for focused ion beam milling of copper, *J. Vac. Sci. Technol. B Microelectron. Nanom. Struct.* 20 (2002) 2682.
- [44] G.K.P. Ramanandan, G. Ramakrishnan, P.C.M. Planken, Oxidation kinetics of nanoscale copper films studied by terahertz transmission spectroscopy, *J. Appl. Phys.* 111 (2012) 123517.
- [45] J.R. Anema, A.G. Brolo, P. Marthandam, R. Gordon, Enhanced Raman scattering from nanoholes in a copper film, *J. Phys. Chem. C* 112 (2008) 17051–17055.
- [46] J.S. Huang, V. Callegari, P. Geisler, C. Brünig, J. Kern, J.C. Prangsma, X. Wu, T. Feichtner, J. Ziegler, P. Weinmann, M. Kamp, A. Forchel, P. Biagioni, U. Sennhauser, B. Hecht, Atomically flat single-crystalline gold nanostructures for plasmonic nanocircuitry, *Nat. Commun.* 1 (2010) 150.
- [47] M. Kuttge, E.J.R. Vesseur, J. Verhoeven, H.J. Lezec, H.A. Atwater, A. Polman, Loss mechanisms of surface plasmon polaritons on gold probed by cathodoluminescence imaging spectroscopy, *Appl. Phys. Lett.* 93 (2008) 113110.
- [48] K.P. Chen, V.P. Drachev, J.D. Borneman, A.V. Kildishev, V.M. Shalae, Drude relaxation rate in grained gold nanoantennas, *Nano Lett.* 10 (2010) 916–922.
- [49] J.H. Park, P. Ambwani, M. Manno, N.C. Lindquist, P. Nagpal, S.H. Oh, C. Leighton, D.J. Norris, Single-crystalline silver films for plasmonics, *Adv. Mater.* 24 (2012) 3988–3992.
- [50] P.R. West, S. Ishii, G.V. Naik, N.K. Emani, V.M. Shalae, A. Boltasseva, Searching for better plasmonic materials, *Laser Photonics Rev.* 4 (2010) 795–808.
- [51] A. Emboras, A. Najjar, S. Nambiar, P. Grosse, E. Augendre, C. Leroux, B. de Salvo, R.E. de Lamaestre, MNOS stack for reliable, low optical loss, Cu based CMOS plasmonic devices, *Opt. Express* 20 (2012) 13612.
- [52] W.P. Chen, J.M. Chen, Use of surface plasma waves for determination of the thickness and optical constants of thin metallic films, *J. Opt. Soc. Am.* 71 (1981) 189.
- [53] G. Baysinger, CRC Handbook of Chemistry and Physics, 79th ed., CRC, Cleveland, Ohio, 2014.
- [54] E.D. Palik, Handbook of Optical Constants of Solids, Elsevier Science, 1997.
- [55] E. Kretschmann, Decay of non radiative surface plasmons into light on rough silver films. Comparison of experimental and theoretical results, *Opt. Commun.* 6 (1972) 185–187.
- [56] R. Karlsson, A. Michaelsson, L. Mattsson, Kinetic analysis of monoclonal antibody-antigen interactions with a new biosensor based analytical system, *J. Immunol. Meth.* 145 (1991) 229–240.
- [57] Y. Tang, X. Zeng, J. Liang, Surface plasmon resonance: An introduction to a surface spectroscopy technique, *J. Chem. Educ.* 87 (2010) 742–746.
- [58] H.H. Nguyen, J. Park, S. Kang, M. Kim, Surface plasmon resonance: A versatile technique for biosensor applications, *Sensors* 15 (2015) 10481–10510.
- [59] J.P. Benedict, R. Anderson, S.J. Klepeis, M. Chaker, A procedure for cross sectioning specific semiconductor devices for both SEM and TEM analysis, *MRS Proc.* 199 (1990) 189–204.
- [60] X. Chen, K. Jiang, Effect of aging on optical properties of bimetallic sensor chips, *Opt. Express* 18 (2010) 1105–1112.
- [61] D.A. McNeill, T. Morrow, P. Dawson, Contrasting damage characteristics in direct incidence and surface plasmon mediated single-shot laser ablation of aluminium films, *Appl. Surf. Sci.* 127–129 (1998) 46–52.
- [62] J. Hyuk Park, P. Nagpal, S.H. Oh, D.J. Norris, Improved dielectric functions in metallic films obtained via template stripping, *Appl. Phys. Lett.* 100 (2012) 81105.
- [63] T.W. Ebbesen, H.J. Lezec, H.F. Ghaemi, T. Thio, P.A. Wolff, Extraordinary optical transmission through sub-wavelength hole arrays, *Nature* 391 (1998) 667–669.
- [64] F.J. Garcia-Vidal, L. Martin-Moreno, T.W. Ebbesen, L. Kuipers, Light passing through subwavelength apertures, *Rev. Mod. Phys.* 82 (2010) 729–787.
- [65] L. Martin-Moreno, F.J. Garcia-Vidal, H.J. Lezec, K.M. Pellerin, T. Thio, J.B. Pendry, T.W. Ebbesen, Theory of extraordinary optical transmission through subwavelength

- hole arrays, Phys. Rev. Lett. 86 (2001) 1114.
- [66] X.T. Geng, B.J. Chun, J.H. Seo, K. Seo, H. Yoon, Frequency comb transferred by surface plasmon resonance, Nat. Commun. 7 (2016) 1–23.
 - [67] H. Ghaemi, T. Thio, D. Grupp, T. Ebbesen, Surface plasmons enhance optical transmission through subwavelength holes, Phys. Rev. B 58 (1998) 6779–6782.
 - [68] J.M. McMahon, J. Henzie, T.W. Odom, G.C. Schatz, S.K. Gray, Tailoring the sensing capabilities of nanohole arrays in gold films with Rayleigh anomaly-surface plasmon polaritons, Opt. Express 15 (2007) 18119.
 - [69] C. Genet, M. van Exter, J. Woerdman, Fano-type interpretation of red shifts and red tails in hole array transmission spectra, Opt. Commun. 225 (2003) 331–336.
 - [70] B.H. Li, C.E. Sanders, J. McIlhargey, F. Cheng, C. Gu, G. Zhang, K. Wu, J. Kim, S.H. Mousavi, A.B. Khanikaev, Y.J. Lu, S. Gwo, G. Shvets, C.K. Shih, X. Qiu, Contrast between surface plasmon polariton-mediated extraordinary optical transmission behavior in epitaxial and polycrystalline Ag films in the mid- and far-infrared regimes, Nano Lett. 12 (2012) 6187–6191.
 - [71] B. Wang, L. Gallais, A theoretical investigation of the laser damage threshold of metal multi-dielectric mirrors for high power ultrashort applications, Opt. Express 21 (2013) 14698.
 - [72] D.J. Miller, M.C. Biesinger, N.S. McIntyre, Interactions of CO₂ and CO at fractional atmosphere pressures with iron and iron oxide surfaces: one possible mechanism for surface contamination? Surf. Interface Anal. 33 (2002) 299–305.